A direct inverse scattering method for imaging obstacles with unknown surface conditions

ANDREW N. NORRIS

Rutgers University, 98 Brett Road, Piscataway, New Jersey 08854-8058, USA

[Received 25 November 1997]

A new technique is described for imaging obstacles using the acoustic far field response for plane wave incidence. The method requires no a priori information about the surface, nor does it depend upon prior knowledge of the surface boundary conditions. The algorithm is straightforward to implement and is illustrated by imaging multiple targets simultaneously for various surface boundary conditions: soft, hard, and impedance. The input data is the full acoustic scattering matrix at a single frequency, from which the eigenvalues and eigenfunctions of the far field operator are determined. Associated incident wave functions are then used to compute a spatial indicator function which takes on large values in the exterior of the target but is bounded inside the obstacle, or obstacles when there are multiple disconnected surfaces.

1. Introduction

Inverse scattering methods may be categorized as direct or indirect, depending upon how the algorithm arrives at the unknown quantity. Here we consider the target identification problem: to find the surface or surfaces of targets given the far field data. Indirect approaches to this problem include optimization or least squares methods, based on an assumed form for the surface. The error between the predicted and measured data is minimized over the class of assumed surfaces, using a direct scattering solver at each step of the solution. Examples on this approach are Angell *et al.* (1989,1997) who use an alternating iteration procedure. This has the advantage that only limited data are needed, but it requires prior knowledge of the target: the assumption that it is a single closed surface with known impedance boundary condition. A related method for obstacle reconstruction is described by Roy *et al.* (1997) which also requires solving the direct problem iteratively. The method of Kirsch and Kress (Colton & Kress 1992) is more direct in that it seeks a closed surface on which the total field satisfies the boundary condition. The related 'dual space' procedure of Colton & Monk (Colton & Kress 1992; Colton & Monk 1994; Misici & Zirilli 1994) also depends critically on knowledge of the surface boundary condition.

Target recognition of underwater and buried marine objects involves reconstructing the exterior surfaces of structures that are themselves wave bearing. At the simplest level, they may be considered to possess frequency dependent surface impedance. Thus, even a sphere of tungsten carbide in water can appear to be acoustically 'soft' at certain frequencies (Norris 1990). Structures comprising metallic plates must be modelled, at the very least, by an impedance condition which depends upon the thickness and the ratio of the mass densities. Given these unavoidable mechanical circumstances, and the sensitivity of the mentioned reconstruction methods to the assumed surface conditions, the target recognition problem

for thick or thin shell objects appears to be a formidable task. This is particularly so if the target consists of two or more closely spaced objects—a veritable clutter of unknown complexity.

The inverse method presented here is radically different from those outlined above. It does not require any assumptions about the surface, which may consist of several disconnected parts. Nor does it presuppose knowledge of the surface boundary conditions (hard, soft or impedance). The price to be paid is that more data are necessary, in the form of extensive far field amplitude and phase information, although only at a single frequency. The output is not a surface but a spatial function which takes on special values for positions inside the target, thereby enabling the boundary or boundaries to be determined. The key to the approach is the ability to infer the eigenvalues and eigenfunctions of the far field operator. The former describe the scattering strength of the target with respect to the associated incident wavefunction, which is defined by the eigenfunction. The eigenvalues cluster about zero, which is the unique point of accumulation, and the associated incident wavefunctions tend to zero on the domain of the target. The present approach does not, as mentioned above, demand prior knowledge of the boundary conditions. In fact, the procedure will be demonstrated for non-simply-connected targets comprising separated multiple scatterers. The reason why this can be achieved is related to the zeroing property of the incident wavefunctions.

Several developments have had particular influences on the present approach. Thus, Colton & Kirsch (1996) demonstrated that it is possible to synthesize scattering from point sources by superposing far field data. This leads to a spatially dependent function which, according to Colton & Kirsch, is singular on the obstacle surface, but bounded elsewhere. More recently, Mast *et al.* (1997) showed that the eigenfunctions of the far field operator form a natural basis for representing distributed inhomogeneities. Their interests were in reconstructing compressibility variations in an acoustic medium. The ideas of Colton & Kirsch (1996) and of Mast *et al.* (1997) are combined here by synthesizing point-source-type fields using functions related to the eigenfunctions of the far field operator. The general procedure is to obtain spatial functions which have characteristic behaviours on the surface of the scatterer. This could be in the form of a singularity at the surface, as in Colton & Kirsch (1996). Alternatively, Potthast (1996) discussed a different procedure for generating a function that becomes singular on the boundary. Here we will derive a spatially dependent function which is unbounded in the exterior but finite in the interior.

We begin with a detailed overview of the far field operator, its properties, and its spectral description. The basic imaging method is introduced in Section 3, and its capacity for reconstructing obstacles using far field data is illustrated via numerical examples in Section 4.

2. The far field operator and its spectral properties

2.1 The far field operator

The total acoustic pressure for a time harmonic wave, with $e^{-i\omega t}$ dependence, due to a plane wave of amplitude p_0 incident in direction α is

$$p(\mathbf{x}) = p_0 e^{ik\alpha \cdot \mathbf{x}} + p^s(\mathbf{x}), \qquad (2.1)$$

where $k = \omega/c$ and c > 0 is the constant wave speed outside the target. The scattered pressure, p^s , is a solution to the homogeneous Helmholtz equation in the exterior of the target or targets, such that the total field satisfies

$$\nabla^2 p + k^2 p = 0, \text{ for } \mathbf{x} \text{ outside } B, \tag{2.2}$$

where B denotes the target boundary The scattered pressure is a radiating or outgoing field at infinity, and the total pressure satisfies certain boundary conditions on B. To be specific, we consider the impedance condition

$$p + \gamma(\mathbf{x}) \frac{\partial p}{\partial n} = 0, \quad \mathbf{x} \in B,$$
 (2.3)

for real γ . For instance, the mass loading of a thin shell of thickness h yields $\gamma = -h\rho_s/\rho_f$, where ρ_s and ρ_f are the solid and fluid densities, respectively. We consider two-dimensional problems only, for which the far field function $u_\infty(\theta,\alpha)$ is defined by the far field behavior of the scattered wave,

$$p^{s}(r,\theta) = -\sqrt{\frac{8\pi}{kr}} e^{i(kr - \frac{1}{4}\pi)} p_0 u_{\infty}(\theta,\alpha) + o\left(\frac{1}{\sqrt{kr}}\right), \quad r \to \infty.$$
 (2.4)

The associated far field operator is

$$U_{\infty} f \equiv \int_{0}^{2\pi} d\alpha \, u_{\infty}(\theta, \alpha) f(\alpha) \,, \tag{2.5}$$

and its transpose is

$$U_{\infty}^* f \equiv \int_0^{2\pi} d\theta \, u_{\infty}^*(\theta, \alpha) f(\theta) \,, \tag{2.6}$$

where u_{∞}^* is the complex conjugate. Note that U_{∞} is related to the operator A of Mast et al. (1997) by $U_{\infty}=\mathrm{i}A/8\pi$, and $-U_{\infty}$ is equivalent to the T-matrix (Waterman 1968). The product $U_{\infty}^*U_{\infty}$ is essentially the time reversal operator of Prada et al. (1995).

The function u_{∞} and the operator U_{∞} satisfy some general properties. First, we note the reciprocal identity that u_{∞} is unaltered under the interchange $(\theta, \alpha) \to (-\alpha, -\theta)$, which is a consequence of source-receiver reciprocity applied in the far field. For two-dimensional scattering, this implies that

$$u_{\infty}(\theta, \alpha) = u_{\infty}(\alpha + \pi, \theta + \pi).$$
 (2.7)

Next, consider the total field resulting from two incident plane waves such that $p(\mathbf{x}) = P(p_1, \boldsymbol{\alpha}; p_2, \boldsymbol{\beta}; \mathbf{x})$, where

$$P(p_1, \boldsymbol{\alpha}; p_2, \boldsymbol{\beta}; \mathbf{x}) \equiv p_1 e^{ik\boldsymbol{\alpha}.\mathbf{x}} + p_2 e^{ik\boldsymbol{\beta}.\mathbf{x}} + p^s(\mathbf{x}). \tag{2.8}$$

The averaged energy flux per cycle at a point is $\frac{1}{2} \text{Re } p^* \mathbf{v}$, where $\mathbf{v} = (\mathrm{i}\omega \rho_f)^{-1} \nabla p$ is the

particle velocity, and therefore the total flux leaving a circle of large radius is \mathcal{F} , where

$$\frac{\omega \rho_f}{2\pi} \mathcal{F} = \frac{\omega \rho_f}{2\pi} \lim_{r \to \infty} \int_0^{2\pi} r d\theta \operatorname{Re} \left(\frac{-ip^*}{2\omega \rho_f} \frac{\partial p}{\partial r} \right)
= \left[2(U_{\infty}^* u_{\infty})(\alpha, \alpha) - u_{\infty}(\alpha, \alpha) - u_{\infty}^*(\alpha, \alpha) \right] |p_1|^2
+ \left[2(U_{\infty}^* u_{\infty})(\beta, \beta) - u_{\infty}(\beta, \beta) - u_{\infty}^*(\beta, \beta) \right] |p_2|^2
+ \left[2(U_{\infty}^* u_{\infty})(\alpha, \beta) - u_{\infty}(\alpha, \beta) - u_{\infty}^*(\beta, \alpha) \right] p_1^* p_2
+ \left[2(U_{\infty}^* u_{\infty})(\beta, \alpha) - u_{\infty}(\beta, \alpha) - u_{\infty}^*(\alpha, \beta) \right] p_1 p_2^* .$$
(2.9)

It is assumed that there is no dissipation in the scattering process, and hence the total energy flux across a closed surface must be zero when averaged over a cycle. In particular $\mathcal{F} = 0$, and consequently each of the four bracketed terms in (2.9) must be zero because of the independence of the complex numbers p_1 and p_2 . Referring to either of the two final terms, and interpreting them as operators, we see that

$$2U_{\infty}^* U_{\infty} - U_{\infty}^* - U_{\infty} = 0, \qquad (2.10)$$

or

$$S^*S = I, (2.11)$$

where S is the scattering operator,

$$S = I - 2U_{\infty} \,, \tag{2.12}$$

and I is the identity, with integrand $\delta(\theta-\alpha)$. If we perform the same flux analysis for the total field $p(\mathbf{x}) = P(p_1, -\boldsymbol{\alpha}; p_2, -\boldsymbol{\beta}; \mathbf{x})$, but replace u_{∞} everywhere that it occurs by using the reciprocal identity (2.7), then we arive at a result similar to equation (2.10) except that $U_{\infty}^* U_{\infty}$ is replaced by $U_{\infty} U_{\infty}^*$. Hence,

$$SS^* = I, (2.13)$$

and we have the important but well-known results that the scattering operator S is unitary and the far field operator U_{∞} is normal (Colton & Kress 1992),

$$U_{\infty}^* U_{\infty} = U_{\infty} U_{\infty}^* \,. \tag{2.14}$$

Let λ be an eigenvalue of U_{∞} with eigenfunction $f(\alpha)$,

$$U_{\infty} f = \lambda f. \tag{2.15}$$

The unitary nature of S implies that λ lies on the circle in the complex plane centred at $\frac{1}{2}$ of radius $\frac{1}{2}$. That is,

$$\lambda = e^{-i\psi} \cos \psi \,, \tag{2.16}$$

for some real angle ψ . We emphasize that the present analysis assumes a lossless medium, Im k = 0; the properties of the eigenvalues are different if absorption is present, as

discussed by Colton & Kress (1995). The set of eigenfunctions $\{f_n\}$, with eigenvalues λ_n , n = 1, 2, 3,..., are assumed to be normalized with respect to the inner product

$$(g, h) = \int_{0}^{2\pi} d\alpha \ g^*(\alpha)h(\alpha), \qquad (2.17)$$

that is, $(f_n, f_m) = \delta_{nm}$. The far field eigenfunctions thus form an orthonormal basis for $L^2[0, 2\pi]$, such that

$$\delta(\theta - \alpha) = \sum_{n} f_n(\theta) f_n^*(\alpha), \qquad u_{\infty}(\theta, \alpha) = \sum_{n} \lambda_n f_n(\theta) f_n^*(\alpha). \tag{2.18}$$

2.2 Incident wavefunctions

The incident field for the eigenfunction f_n is defined as

$$E_n(\mathbf{x}) = \left(e^{-ik\alpha \cdot \mathbf{x}}, \ f_n(\alpha) \right). \tag{2.19}$$

The associated far field is $u_{\infty} = U_{\infty} f_n$, which reduces to $u_{\infty} = \lambda_n f_n$, so that the total field is

$$p(r,\theta) = E_n(\mathbf{x}) - \sqrt{\frac{8\pi}{kr}} e^{\mathrm{i}(kr - \frac{1}{4}\pi)} \lambda_n f_n(\theta) + \left(\frac{1}{\sqrt{kr}}\right), \quad r \to \infty.$$
 (2.20)

Hence, $E_n(\mathbf{x})$ is the unique incident wave which has the far field $f_n(\theta)$. It is useful to list some of the properties of the incident wavefunctions $\{E_n\}$. First, they form a basis for plane waves, which may be deduced using $(2.18)_1$,

$$e^{ik\boldsymbol{\alpha}.\mathbf{x}} = \sum_{n} E_{n}(\mathbf{x}) f_{n}^{*}(\alpha). \qquad (2.21)$$

Using the identity $(e^{ik\boldsymbol{\alpha}.\mathbf{y}}, e^{ik\boldsymbol{\alpha}.\mathbf{x}}) = 2\pi J_0(k|\mathbf{x} - \mathbf{y}|)$, equation (2.21) implies that

$$2\pi J_0(k|\mathbf{x} - \mathbf{y}|) = \sum_n E_n(\mathbf{x}) E_n^*(\mathbf{y}).$$
 (2.22)

Let us see how the choice of the origin determines the eigenfunctions. The far field function with respect to a new or shifted origin at $\mathbf{x}^{(s)}$ is

$$u_{\infty}^{(s)}(\theta,\alpha) = e^{ik\theta \cdot \mathbf{x}^{(s)}} u_{\infty}(\theta,\alpha) e^{-ik\alpha \cdot \mathbf{x}^{(s)}}.$$
 (2.23)

The modified eigenvalues are therefore the same as before, $\lambda_n^{(s)} = \lambda_n$, but the far field eigenfunctions are changed, to

$$f_n^{(s)}(\theta) = e^{ik\theta \cdot \mathbf{x}^{(s)}} f_n(\theta). \qquad (2.24)$$

However, the modified incident fields, defined with respect to the shifted origin, are

$$E_n^{(s)}(\mathbf{x}) = \left(e^{-ik\boldsymbol{\alpha}.(\mathbf{x}-\mathbf{x}^{(s)})}, f_n^{(s)}(\alpha)\right)$$

= $E_n(\mathbf{x})$, (2.25)

where we have used (2.19). In summary, the far field eigenfunctions $f_n^{(s)}$ depend upon the choice of origin, but the incident fields E_n are independent of the origin.

The fact that the incident wavefunctions form a representation for plane waves means that they are not spatially compact. This may be seen by considering the integral of $E_n(\mathbf{x})$ over the interior of the circle of radius R, which can be found using standard identities for Bessel functions and their integrals,

$$\int_{r \le R} d\mathbf{x} \, E_n(\mathbf{x}) = 2\pi \, \frac{R}{k} J_1(kR) \, (1, f_n) \,. \tag{2.26}$$

This is not defined in the limit as $R \to \infty$. Alternatively, let us consider the 'inner product' on the interior of the same circle:

$$I_{mn}(R) = \int_{r \leq R} d\mathbf{x} \, E_m(\mathbf{x}) E_n^*(\mathbf{x}). \tag{2.27}$$

This may be simplified, using (2.19) and the Bessel function identities once more:

$$I_{mn}(R) = \int_{0}^{2\pi} d\alpha \int_{0}^{2\pi} d\beta f_{m}(\alpha) f_{n}^{*}(\beta) \int_{0}^{R} r dr \int_{0}^{2\pi} d\theta e^{ikr\cos(\alpha - \beta)}$$

$$= 2\pi \frac{R}{k} \int_{0}^{2\pi} d\alpha \int_{0}^{2\pi} d\beta f_{m}(\alpha) f_{n}^{*}(\beta) \frac{J_{1}(kR|\alpha - \beta|)}{|\alpha - \beta|}.$$
(2.28)

For large R we may use the equivalence $J_1(kR|\boldsymbol{\alpha}-\boldsymbol{\beta}|)/|\boldsymbol{\alpha}-\boldsymbol{\beta}|\approx 2\delta(\alpha-\beta)$, to obtain

$$I_{mn}(R) = 4\pi \frac{R}{k} \delta_{mn} + O(1)$$
. (2.29)

Thus, the incident wavefunctions are orthogonal on large domains.

Zero eigenvalues can occur, and they have a direct physical interpretation: Interior resonance frequencies correspond to zeros of the far field operator. In order to prove this statement, suppose that $p_0(\mathbf{x})$ is a mode of the interior problem, that is, a solution of the Helmholtz equation inside B subject to the impedance condition (2.3) on the boundary. This may be expanded as

$$p_0(\mathbf{x}) = \sum_{n = -\infty}^{\infty} c_n J_n(kr) e^{in\theta} , \text{ for } \mathbf{x} \text{ inside } B,$$
 (2.30)

for some constants $\{c_n\}$. This representation of the interior mode, valid for \mathbf{x} inside B, can now be continued to the exterior. Thus, the incident field

$$E(\mathbf{x}) \equiv \sum_{n=-\infty}^{\infty} c_n J_n(kr) e^{in\theta} , \text{ for } \mathbf{x} \text{ outside } B,$$
 (2.31)

automatically satisfies the boundary condition (2.3), and it therefore corresponds to a far field eigenfunction with eigenvalue zero. The eigenfunction follows from (2.31) as

$$f(\theta) = b \sum_{n = -\infty}^{\infty} c_n (-i)^n e^{in\theta}, \qquad (2.32)$$

where b is a normalization factor.

The existence of zero eigenvalues is well known, but they occur only at discrete frequencies. However, no matter what frequency we consider, zero is a point of accumulation for eigenvalues, meaning that for any $\epsilon > 0$ there exists an infinite set of eigenvalues of magnitude less than ϵ . The physical meaning of these is quite distinct from the possible zero eigenvalue: they result from the fact that the far field operator is compact. Eigenfunctions with λ_n close to zero possess incident fields which generate extremely weak scattered far fields, and are thus difficult to extricate from the far field response. The sensitivity of these functions to the far field data is a direct indication of the ill-posed nature of the inverse scattering problem.

2.3 Example: The circle

As an example, consider a circular target, B: r = a, with a constant surface impedance γ . The eigenvalues are given by equation (2.16) with

$$\psi_n = \arg\left(H_n^{(1)}(ka) + k\gamma H_n^{(1)}(ka)\right). \tag{2.33}$$

The eigenfunctions and associated incident fields are

$$f_n(\theta) = \frac{1}{\sqrt{2\pi}} e^{in\theta}, \qquad E_n(\mathbf{x}) = \sqrt{2\pi} i^n J_n(kr) e^{in\theta}.$$
 (2.34)

This example indicates that the eigenfunction can be quite independent of the eigenvalue. That is, for a given eigenfunction, f_n , the eigenvalue can take on any value on the circle of eigenvalues. For example, by varying the surface impedance γ one can change each eigenvalue for the circle, but the eigenfunctions remain fixed. Thus, the magnitude of λ_n has little or no bearing on the focusing property of the eigenfunction f_n . This is perhaps contrary to the statements of Mast *et al.* (1997) concerning focusing and eigenfunctions of the far field operator; although their objective was quite different, as they were interested in smoothly varying materials rather than sharp interfaces.

This simple example illustrates the remark above that zeros of λ_n correspond to resonance frequencies of the interior problem, because in this case they occur when

$$J_n(ka) + k\gamma J'_n(ka) = 0 \quad \Leftrightarrow \quad \lambda_n = 0. \tag{2.35}$$

We note that (2.22) directly gives the well-known identity for Bessel functions:

$$J_0(k|\mathbf{x}_1 - \mathbf{x}_2|) = \sum_{n = -\infty}^{\infty} J_n(kr_1) J_n(kr_2) e^{in(\theta_1 - \theta_2)}.$$
 (2.36)

Also, the inner products of (2.27) are explicit in this case,

$$I_{mn}(R) = \delta_{mn} \, 2\pi^2 R^2 \left[J_n^2(kR) - J_{n-1}(kR) J_{n+1}(kR) \right], \tag{2.37}$$

thus verifying the approximation (2.29) for large R.

3. The imaging algorithm

Suppose we are given a far field pattern, $F(\theta)$, such that the total acoustic pressure is

$$p(r,\theta) = G(\mathbf{x}) - \sqrt{\frac{8\pi}{kr}} e^{\mathrm{i}(kr - \frac{1}{4}\pi)} F(\theta) + o\left(\frac{1}{\sqrt{kr}}\right), \quad r \to \infty.$$
 (3.38)

Can we determine the incident field G uniquely? The answer is no because the near-to-far field operator is compact and hence has no inverse. In order to see this, suppose we expand F in terms of the far field eigenfunctions, using $(2.18)_1$,

$$F(\theta) = \sum_{n} f_n(\theta) (f_n, F).$$
 (3.39)

This is well defined, but the function

$$\sum_{n} \frac{1}{\lambda_n} f_n(\theta) \left(f_n, F \right) \tag{3.40}$$

is not, because of the property that the eigenvalues cluster about zero. This is directly related to the fact that U_{∞} is not invertible. However, the truncated function

$$g^{(N)}(\theta) = \sum_{n=1}^{N} \frac{1}{\lambda_n} f_n(\theta) \left(f_n, F \right)$$
(3.41)

is a suitable approximation. The associated incident field

$$G^{(N)}(\mathbf{x}) = \left(e^{-ik\boldsymbol{\alpha}.\mathbf{x}}, \ g^{(N)}(\boldsymbol{\alpha})\right) = \sum_{n=1}^{N} \frac{1}{\lambda_n} E_n(\mathbf{x}) \left(f_n, \ F\right), \tag{3.42}$$

is a regularized solution to the problem of finding G of (3.38), using a spectral cut-off regularization (Colton & Kress 1992).

We now apply this regularization procedure to far field patterns associated with point source incident fields. These are far fields which would arise from a monopole or multipole at source point y. The generic case, for a monopole, is $F(\theta) = F(\theta, y)$, where

$$F(\theta, \mathbf{y}) = e^{-ik\theta \cdot \mathbf{y}}.$$
 (3.43)

The regularized incident function follows from (2.19) and (3.41) as

$$g^{(N)}(\theta, \mathbf{y}) = \sum_{n=1}^{N} \frac{1}{\lambda_n} f_n(\theta) E_n^*(\mathbf{y}), \qquad (3.44)$$

and the incident field is therefore,

$$G^{(N)}(\mathbf{x}, \mathbf{y}) = \sum_{n=1}^{N} \frac{1}{\lambda_n} E_n(\mathbf{x}) E_n^*(\mathbf{y}).$$
 (3.45)

The present technique is closely related to that of Colton & Kirsch (1996), who defined a 'far field equation' for an unknown function $g(\theta, \mathbf{y})$:

$$U_{\infty}g = e^{-ik\theta \cdot y}. \tag{3.46}$$

This integral equation of the first kind cannot be solved in general because U_{∞} is a compact operator. However, by confining \mathbf{y} to some restricted domain and using Tikhonov regularization, Colton & Kirsch obtained numerical solutions to (3.46). They showed that g has a logarithmic singularity when \mathbf{y} lies on the obstacle surface, and based on this a reconstruction algorithm follows by plotting the function $g(\theta, \mathbf{y})$ versus \mathbf{y} ; see also (Colton *et al.* 1997).

The incident wave for the function g of equation (3.46) is

$$G(\mathbf{x}, \mathbf{y}) \equiv (e^{ik\theta \cdot \mathbf{x}}, g(\theta; \mathbf{y}))$$
 (3.47)

which, by definition, has an associated far field pattern $e^{-ik\theta \cdot y}$, or a total solution

$$p(r,\theta) = G(\mathbf{x}, \mathbf{y}) - \sqrt{\frac{8\pi}{kr}} e^{\mathrm{i}(kr - \frac{1}{4}\pi)} e^{-\mathrm{i}k\theta \cdot \mathbf{y}} + o\left(\frac{1}{\sqrt{kr}}\right), \quad r \to \infty.$$
 (3.48)

The unique radiating field with this far field is $p^s = -2\pi H_0^{(1)}(k|\mathbf{x} - \mathbf{y}|)$, which is the scattered field for the incident wave G, implying the total field

$$p(\mathbf{x}, \mathbf{y}) = G(\mathbf{x}, \mathbf{y}) - 2\pi H_0^{(1)}(k|\mathbf{x} - \mathbf{y}|). \tag{3.49}$$

How are we to interpret this? First, it is clear that G of equation (3.47) is the limit of $G^{(N)}$ as $N \to \infty$, if the limit exists. At the same time, if the source point \mathbf{y} is in the exterior region then the incident field which gives rise to the scattered field of (3.49) is simply

$$G(\mathbf{x}, \mathbf{y}) = 2\pi H_0^{(1)}(k|\mathbf{x} - \mathbf{y}|),$$
 (3.50)

and the total field is zero. Hence, as $|\mathbf{x} - \mathbf{y}| \to 0$ the function $G^{(N)}(\mathbf{x}, \mathbf{y})$ should, in some approximate sense, synthesize the singularity of $2\pi H_0^{(1)}(z)$ as $z \to 0$. This suggests that the function $|G^{(N)}(\mathbf{x}, \mathbf{x})|$ should take on large values for *all* \mathbf{x} in the exterior of the target. It is interesting to note the duality between the expression (2.22), on the one hand and

$$2\pi H_0^{(1)}(k|\mathbf{x} - \mathbf{y}|) = \sum_n \frac{1}{\lambda_n} E_n(\mathbf{x}) E_n^*(\mathbf{y}) \text{ for } \mathbf{x} \text{ or } \mathbf{y} \text{ outside } B,$$
 (3.51)

on the other. The latter follows from (3.45) and (3.50) and uses the symmetry of $G^{(N)}$ with respect to **x** and **y** to deduce that (3.51) applies if either one is in the exterior domain.

At the same time, the analysis for the circular target in Appendix A indicates that $|G^{(N)}(\mathbf{x},\mathbf{x})|$ is bounded for positions \mathbf{x} located inside the target. Does this property extend to other, far more complex, target geometries? We claim here that it does, and offer as proof the numerical evidence of the examples in the next section, deferring until later a more rigorous proof, although a brief outline of such is provided in Section 4. The different behaviour of $|G^{(N)}(\mathbf{x},\mathbf{x})|$ for \mathbf{x} inside or outside the target suggests that we try to locate regions of space where this function is small. Such regions indicate the scattering obstacles. Whether or not this is feasible will be evident from the numerical examples next.

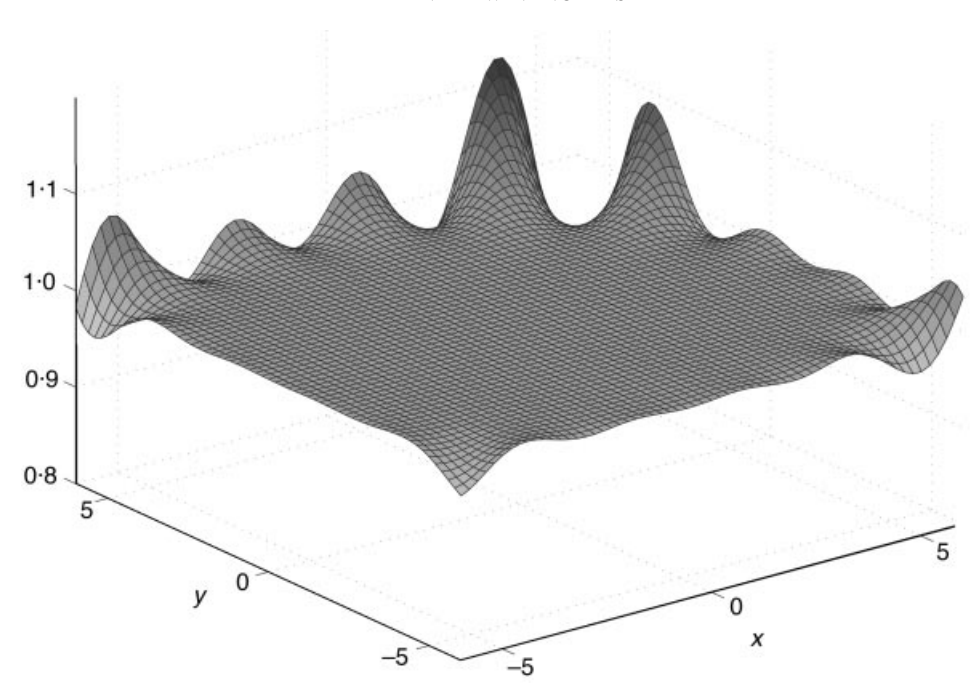


FIG. 1. The calculated function $\widehat{I}(\mathbf{x})$ of (4.57) using the computed incident wavefunctions for the 3-cylinder target at ka=1. The three obstacles are of unit radius and centres (x,y)=(3,-2), (-3,-2) and (-3,2)

4. Numerical experiments and discussion

4.1 Computational method

Given the far field data, $u_{\infty}(\theta, \alpha)$, whether synthetic or otherwise, the far field eigenfunctions are found by taking inner products of the far field operator with the exponential functions $\{(2\pi)^{-1/2}e^{in\theta}\}$. Thus, we form the square matrix [U], such that

$$u_{\infty}(\theta, \alpha) = \frac{1}{2\pi} \sum_{m}^{(M)} \sum_{n}^{(M)} U_{mn} e^{i(m\theta - n\alpha)},$$
 (4.52)

where

$$U_{mn} = \frac{1}{2\pi} \int_{0}^{2\pi} d\theta \int_{0}^{2\pi} d\alpha \, u_{\infty}(\theta, \alpha) e^{-i(m\theta - n\alpha)}. \tag{4.53}$$

The next step is to diagonalize [U] as

$$[U] = [V][\Lambda][V]^*,$$
 (4.54)

such that the columns of [V] are the right eigenvectors of [U], and $[\Lambda]$ is the diagonal eigenvalue matrix,

$$\Lambda_{mn} = \widehat{\lambda}_n \delta_{mn} \,, \tag{4.55}$$

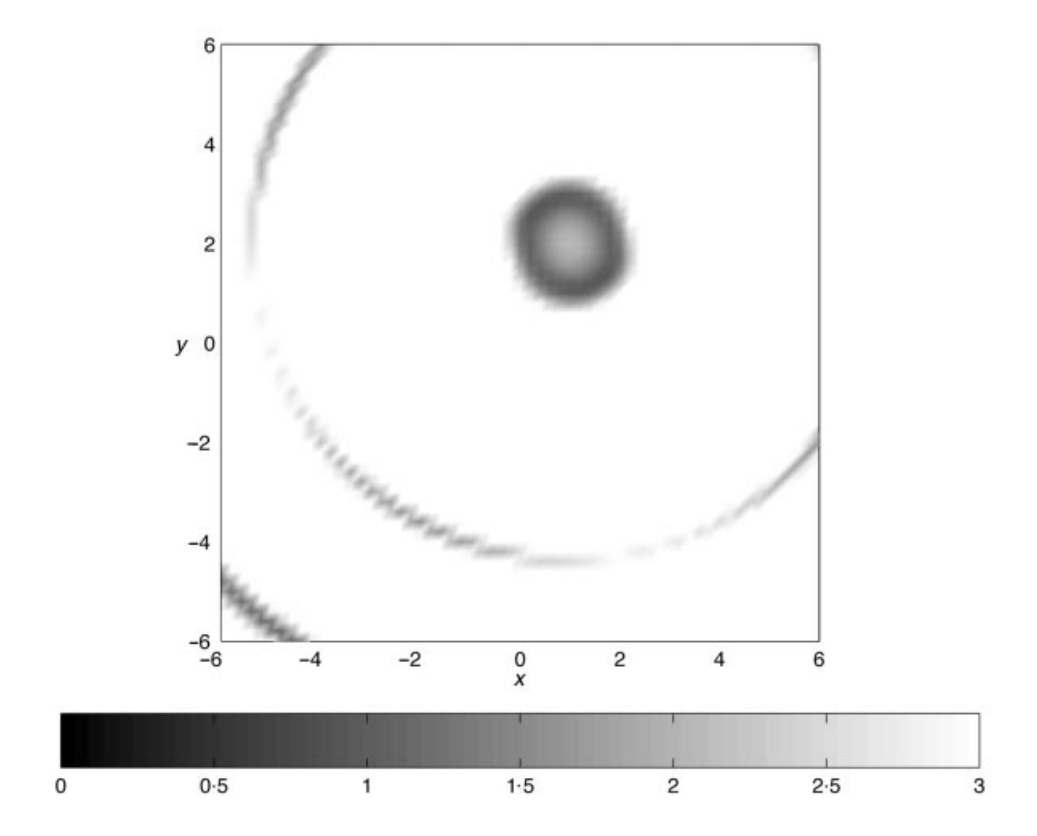


FIG. 2. The image of a circular target of unit radius centered at (x, y) = (1, 2), at ka = 1 with impedance v = 100

where the carat on a quantity indicates that it is an approximant. Also, $[V]^*$ is the Hermitian transpose and it follows that [V] is a unitary matrix. The approximate incident wavefunction is therefore, using (2.34),

$$\widehat{E}_n(\mathbf{x}) = \sum_{m}^{(M)} \sqrt{2\pi} \,\mathbf{i}^m \,J_m(kr) e^{\mathbf{i}m\theta} \,V_{mn} \,. \tag{4.56}$$

In applying the present technique, it is important to first determine how well the approximated eigenfunctions can represent plane waves on the domain of computation, which in the examples considered is the square $-6 \le x$, $y \le 6$. Referring to equation (2.22), we assess this by visual inspection of the function

$$\widehat{I}(\mathbf{x}) = \frac{1}{2\pi} \sum_{n}^{(M)} \widehat{E}_n(\mathbf{x}) \, \widehat{E}_n^*(\mathbf{x}) \,, \tag{4.57}$$

which should be unity or close to it on the domain of interest. Figure 1 shows this for

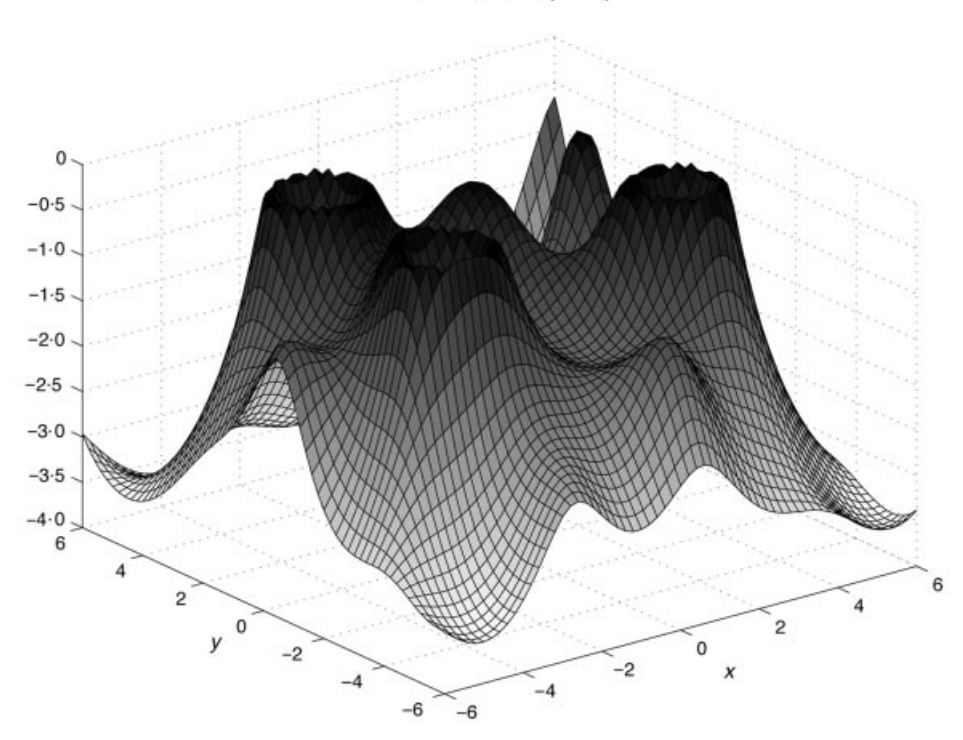


FIG. 3. The surface shows the quantity $-\log |G^{(N)}(\mathbf{x}, \mathbf{x})|$ for the 3-cylinder target with $\gamma = 1000$ and ka = 1

the eigenfunctions of the 3-cylinder target at ka=1 considered below. The accuracy is reasonable over a large region centred on the origin, but deteriorates further away. The limitation here is the number of circular functions employed in generating [U], which is 17 in this example.

4.2 Examples

We consider targets comprising one, two or three circular obstacles, all of unit radius (a=1). The far field of the forward multiple scattering problem is obtained using the procedure outlined in Appendix B. The eigenfunctions and eigenvalues are determined, as described above, and the approximant $\widehat{I}(\mathbf{x})$ is examined; see Fig. 1. Then the 'indicator' function $|G^{(N)}(\mathbf{x},\mathbf{x})|$ is plotted on the domain of interest, $-6 \leqslant x$, $y \leqslant 6$.

The method was first put to the test on the trivial example of a single circular target. Figure 2 shows a grey scale image of the final result: the details of the plotting procedure are outlined below. As a more stringent test we consider a target comprising three distinct circular obstacles of unit radius centred at the points (x, y) = (3, -2), (-3, -2) and (-3, 2). The indicator function $|G^{(N)}(\mathbf{x}, \mathbf{x})|$ of (3.45) is shown in Fig. 3. The quantity plotted versus $\mathbf{x} = (x, y)$ is $z = -\log |G^{(N)}(\mathbf{x}, \mathbf{x})|$, and it is evident from Fig. 3 that the magnitude of $G^{(N)}$ is indeed large at points away from the target domain. It is difficult to discern the demarcations in Fig. 3, so we henceforth illustrate the indicator function by

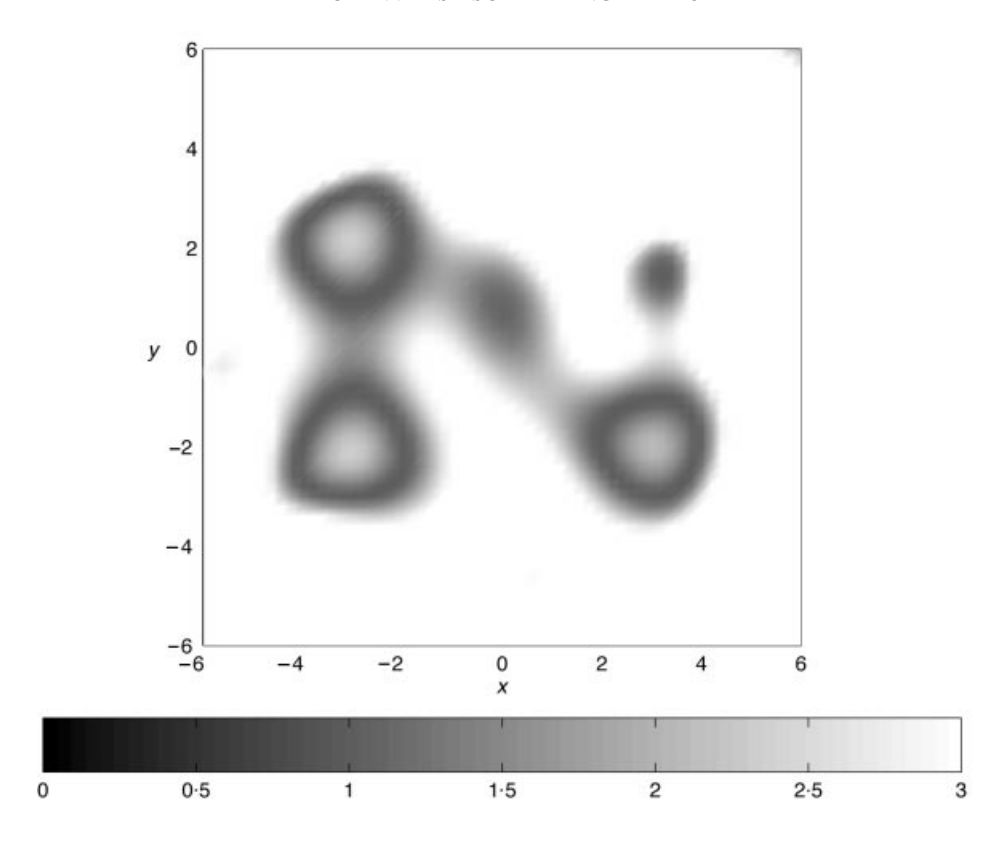


FIG. 4. The grey-scale replica of Fig. 3, on a linear scale

grey-scale images, as in Fig. 2 for the single obstacle. The grey-scale image of Fig. 3 is depicted in Fig. 4, which shows $|G^{(N)}(\mathbf{x},\mathbf{x})|$ on a linear scale with the dark areas showing the regions where the indicator function is small in magnitude. The three circular obstacles are clearly imaged, but several phantom images appear in Fig. 4. The spurious images shift with varying frequency, see Fig. 5, and could be eliminated in practice by using data from more than a single frequency.

Figure 6 shows the computed eigenvalues of the three circular obstacles for ka=1 using circular basis functions $e^{in\theta}$ with $-8\leqslant n\leqslant 8$, yielding a 17×17 matrix [U]. The eigenvalues in Fig. 6 display the expected clustering near zero. All the numerical images, such as Figs 3 to 5 and subsequent ones, were generated by retaining only those eigenvalues of magnitude greater than 10^{-3} for the purpose of evaluating $G^{(N)}$ of equation (3.45). The choice of the spectral cut-off $|\lambda_n|>10^{-3}$ is quite arbitrary, but in general it will depend upon the numerical precision of the data. The same procedure was employed in all results presented here, and it typically meant that about N=10 eigenvalues and eigenfunctions were used in computing $G^{(N)}$. The relevant incident wavefunctions $\{E_n\}$ associated with the nine largest eigenvalues of Fig. 6 are illustrated in Fig. 7. These are the essential basis for the images in Figs 3 to 5.

The four images in Fig. 8 were generated for two identical circular obstacles centred at

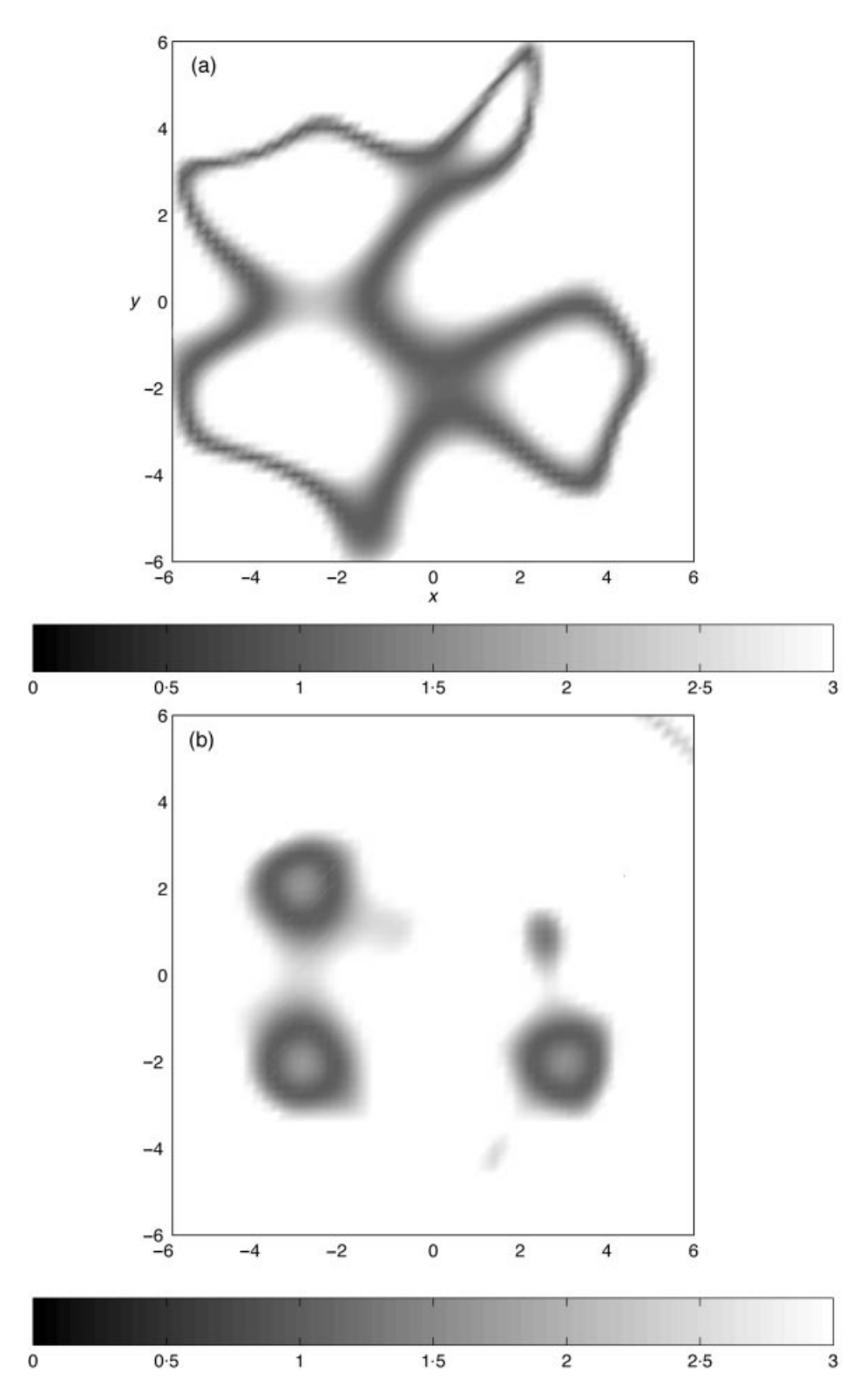


Fig. 5. The same as Fig. 4 but for (a) ka=0.6, and (b) ka=1.2

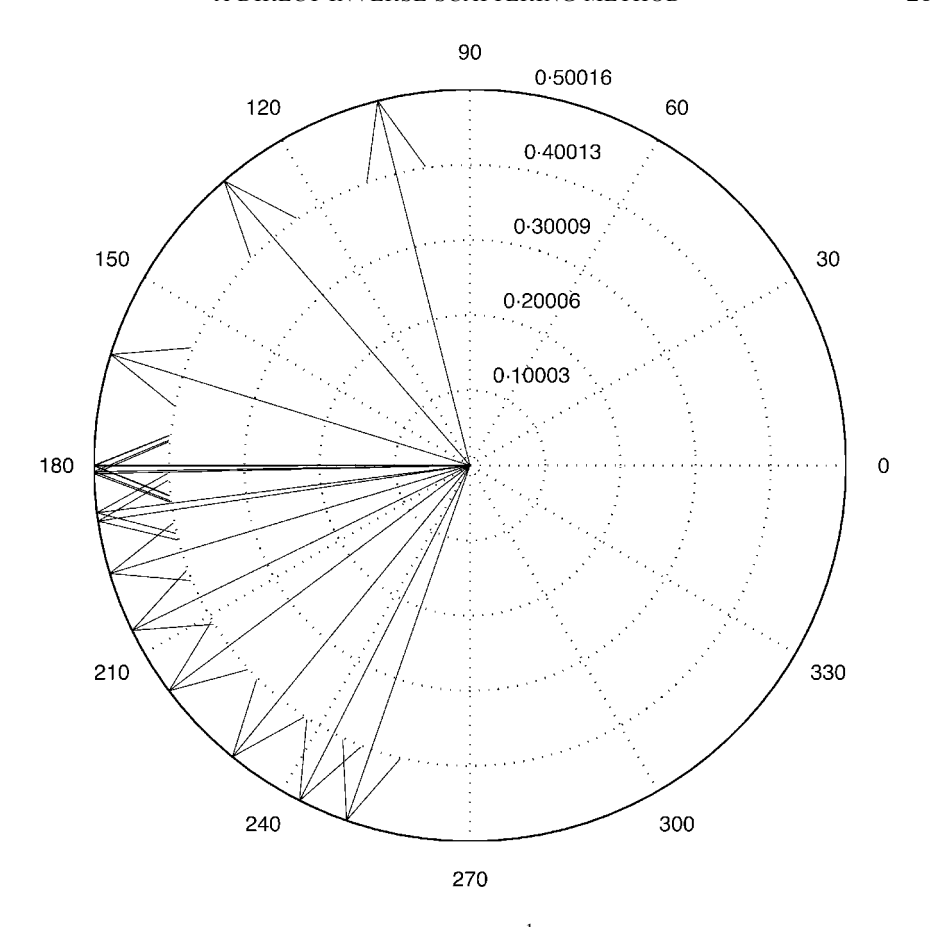


FIG. 6. An Argand diagram of the complex numbers $\lambda_n - \frac{1}{2}$ for the 3-cylinder example with ka = 1 and $\gamma_j = 1000$ (hard obstacles). The matrix [U] is 17×17 implying 17 eigenvalues. The point of accumulation around zero (at 180°) is evident

(x, y) = (-1, -2) and (2, 2) for different surface conditions. Thus, Figs 8a,b correspond to soft $(\gamma = 0)$ and hard $(\gamma = 1000)$ boundary conditions, respectively, both at ka = 1. Image 8c was computed for the mass-like boundary condition $\gamma = -1$ at ka = 1. Spurious images are apparent in 8c, but they are seen to disappear at a different frequency, as image 8d for ka = 0.8 illustrates. However, note the quite distinct intensity scales in 8c and 8d.

4.3 Discussion

The numerical examples demonstrate that the computed indicator function $G^{(N)}(\mathbf{x}, \mathbf{x})$ takes on large values outside the target, and is bounded at or near the target, as claimed in Section 3. The reason for the large values in the exterior domain is that the indicator function attempts to emulate a point source at its source, see (3.50). At the same time, the analysis for the circular target in Appendix A indicates that $G(\mathbf{x}, \mathbf{x})$ is well defined only inside the target, and is divergent outside. However, it is not clear why the indicator func-

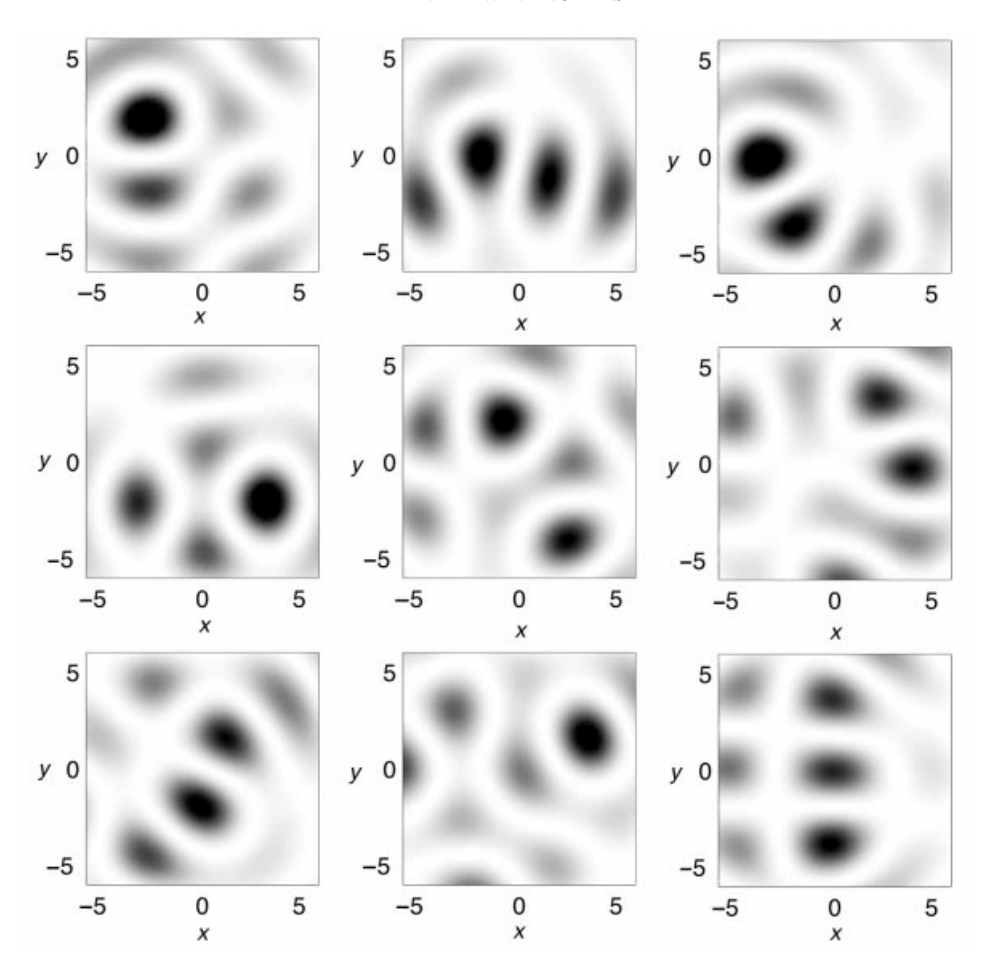


FIG. 7. The first nine incident wavefunctions of the three-obstacle target, associated with the nine largest eigenvalues of Fig. 6. The shading indicates regions where the functions are large in magnitude

tion should, in general, be bounded inside the target. By way of justification, we offer the following physical argument, based on superposition.

The field scattered from an obstacle is regular in the exterior region, but cannot be continued into the interior. However, the scattered field may be represented to a given degree of accuracy by a finite set of virtual sources located *inside* the obstacle. Angell *et al.* (1997) have shown that these sources are linearly independent in the far field, and that such a representation is a suitable basis for solving the forward problem. If we assume that the source amplitudes are linear functions of the incident direction, then by appropriate superposition of incident waves, one can isolate any single virtual source. Thus, a point source at arbitrary location \mathbf{y} inside the target can be synthesized by incident plane waves. Hence the incident field, $G(\mathbf{x}, \mathbf{y})$, is regular at a source location $\mathbf{y} = \mathbf{x}$ inside the target.

A quite different perspective of the method is gained by noting that the incident wavefunctions associated with the accumulating eigenvalues are vanishingly small on the do-

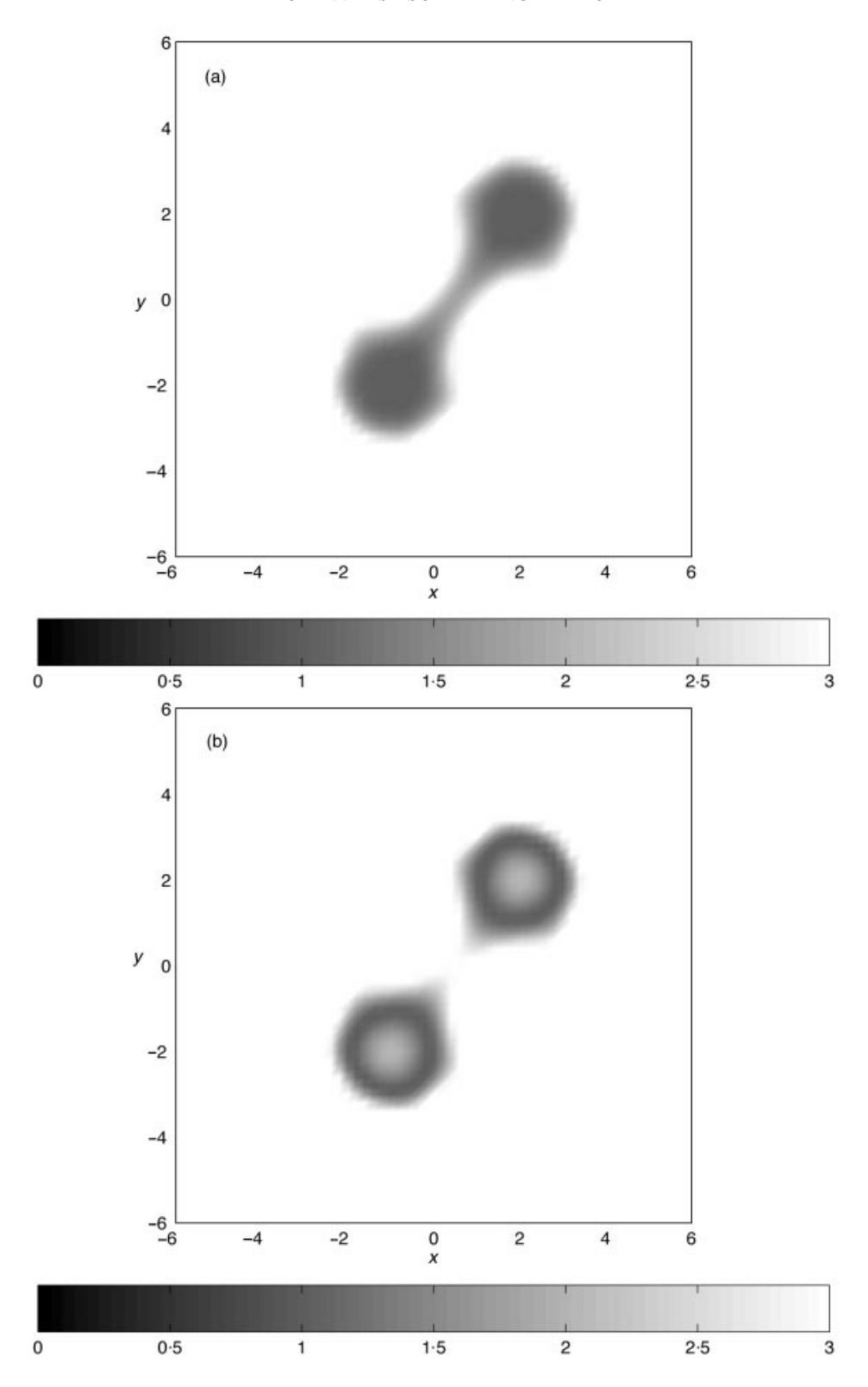


FIG. 8. (a) Two soft ($\gamma=0$) cylinders of unit radius centred at (-1,-2) and (2,2) for ka=1; and (b) The same as (a) but for hard cylinders ($\gamma=1000$)

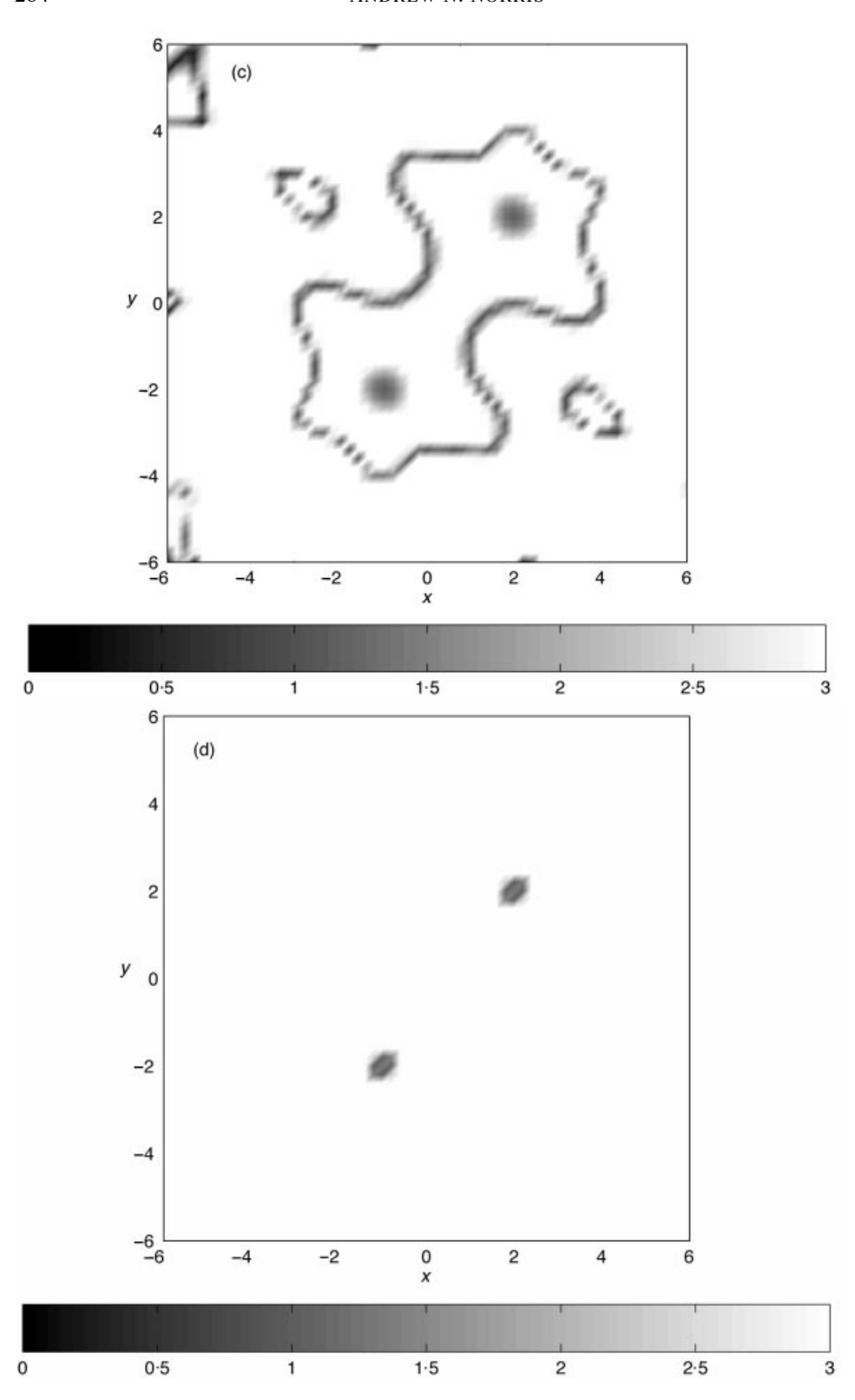
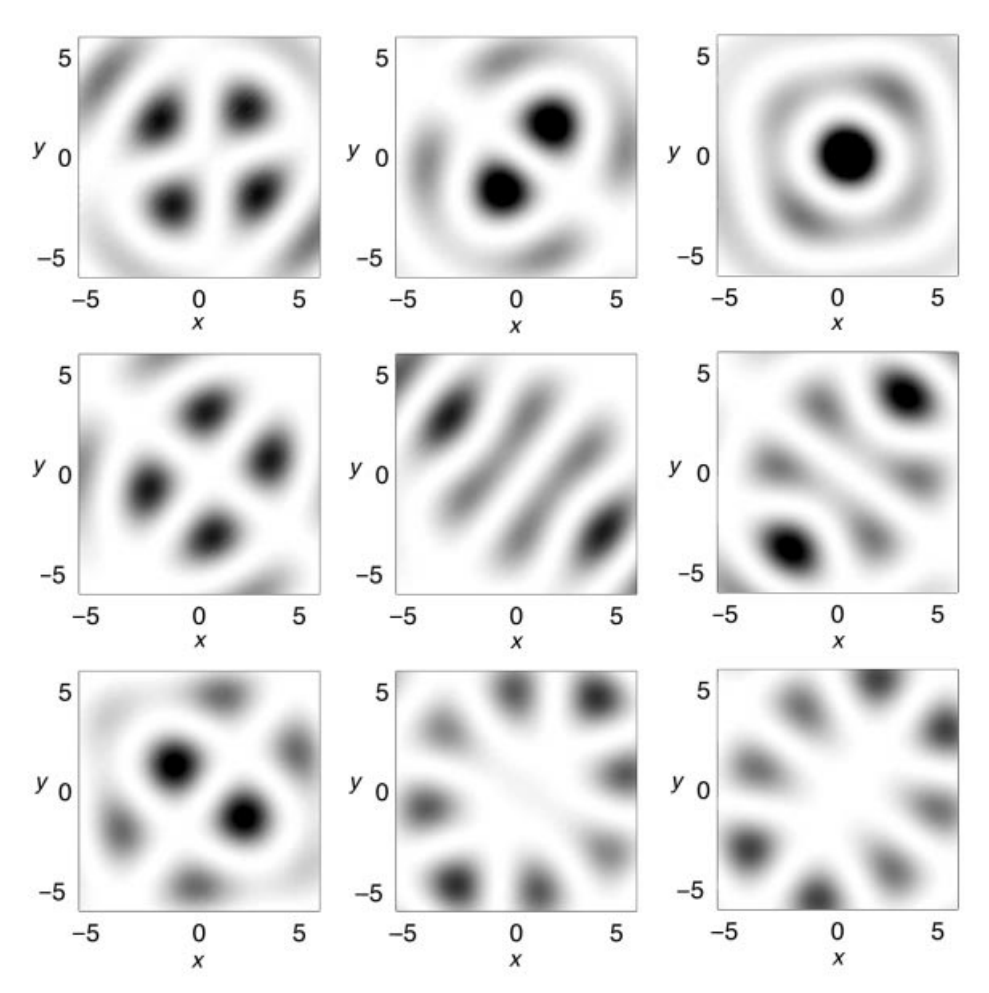


FIG. 8. (c) Two mass-like cylinders ($\gamma=-1$) at ka=1; and (d) The same as (c) but for ka=0.8



 $FIG.\ 9.\ The\ first\ nine\ incident\ wavefunctions\ of\ the\ two-obstacle\ target\ considered\ in\ Fig.\ 8a$

main of the target. This property, what one might call a nullification on the target region, guarantees that the scattered field, and hence λ_n , are both small. In order to appreciate this property, consider the incident wavefunctions corresponding to Figs 8a and 8b, which are shown in Figs 9 and 10, respectively. It is clear that the wavefunctions are similar, despite the different surface conditions, although they are re-ordered because of the quite different eigenvalues for the two solutions. The first few wavefunctions in either case have sizeable amplitudes on the target domain, but for those associated with smaller λ_n (in the lower rows of Figs 9 and 10) it is apparent that the functions are small in magnitude on the target region. This feature is much more apparent if we look at a wavefunction for some very small eigenvalue. Thus, Fig. 11 shows the wavefunction for the 12th largest eigenvalue for image 8b—the pair of hard cylinders (note the scale in Fig. 11!). The fact that these wavefunctions are approximately zero on the target domain, or more specifically, on the

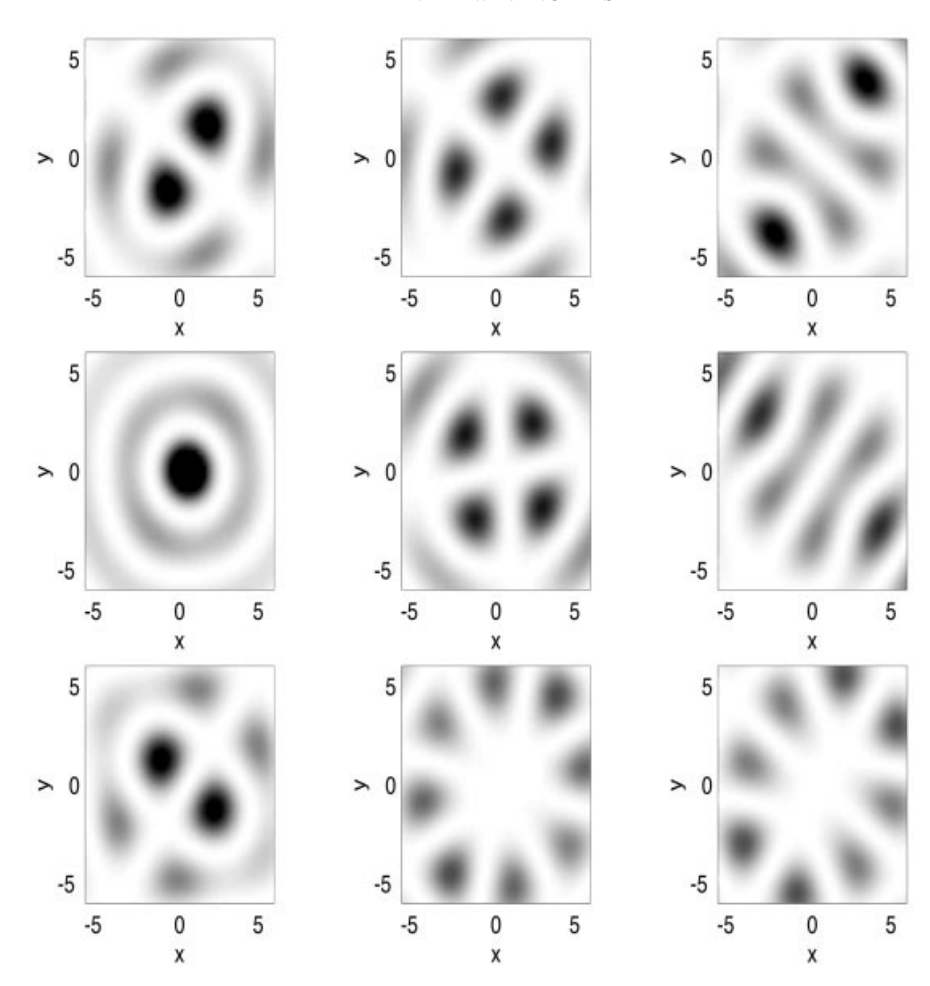


FIG. 10. The first nine incident wavefunctions of the two-obstacle target considered in Fig. 8b

boundary B, suggests that they possess the potential to demarcate the boundary. It is this zeroing property that lies at the heart of the imaging method.

5. Summary

We have demonstrated a new method for using the incident wave functions of the scattering operator to image non-convex, disconnected scatterers, with various surface boundary conditions: hard, soft and finite impedance. The inversion algorithm is direct, with no iteration or forward scattering solver required. The surface boundary conditions do not need to be known in advance, and it is this feature above all else that distinguishes the method from other inversion schemes.

The analysis and examples in this paper are strictly 2-dimensional, but it is clear that the methods can be applied directly to 3-dimensional problems, given the appropriate 3-

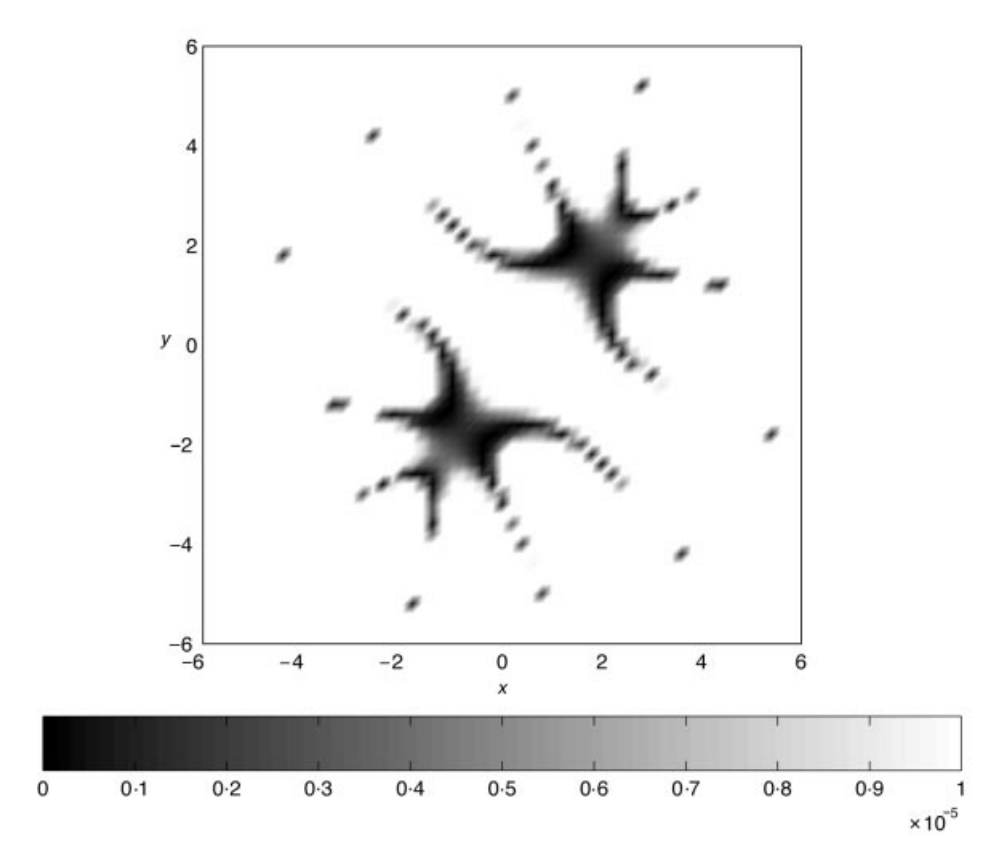


FIG. 11. The incident wavefunction for the 12th eigenvalue of Fig. 8b. In this case the shading indicates where the magnitude of the function is small

dimensional far field data. We have also made no attempt to address questions related to limited aperture far field data, absorption, or sensitivity to noise.

Finally, we remark that the results presented here shed light on the general issues confronting the inverse scatterer seeking unknown targets. It is sometimes convenient to use the language of evanescent fields and complex wavenumbers, both of which are absent from the far field data, but are crucial to the near field, and hence the target identification. Here, however, we demonstrate the importance of the ability to infer the far field eigenvalues, and the related incident wavefunctions. These are contained within the far field operator, but in an ill-conditioned sense because of the asymptotic clustering of the eigenvalues about $\lambda_n = 0$ as $n \to \infty$.

Acknowledgments

The author would like to thank Dr A. Kirsch for providing comments on the manuscript. This work was supported by the Office of Naval Research.

REFERENCES

ANGELL, T. S., KLEINMAN, R. E., & ROACH, G. F. 1989 A constructive method for identification of an impenetrable scatterer. *Wave Motion* 11, 185-200.

ANGELL, T. S., JIANG, X., & KLEINMAN, R. E. 1997 A distributed source method for inverse acoustic scattering. *Inverse Problems* 13, 531-545.

COLTON, D. & KIRSCH, A. 1996 A simple method for solving inverse scattering problems in the resonance region. *Inverse Problems* 12, 383-393.

COLTON, D. & KRESS, R. 1995 Eigenvalues of the far field operator for the Helmholtz equation in an absorbing medium. *SIAM J. Appl. Math.* **55**, 1724-1735.

COLTON, D. & KRESS, R. 1992 Inverse Acoustic and Electromagnetic Scattering Theory. Berlin: Springer.

COLTON, D. & MONK, P. 1994 A modified dual space method for solving the electromagnetic inverse scattering problem for an infinite cylinder. *Inverse Problems* **10**, 87-107.

COLTON, D., PIANA, M., & POTTHAST, R. 1997 A simple method using Morozov's discrepancy principle for solving inverse scattering problems. *Inverse Problems* 13, 1477-1493.

MAST, T. D., NACHMAN, A. I., & WAAG, R. C. 1997 Focusing and imaging using eigenfunctions of the scattering operator. *J. Acoust. Soc. Am.* 102, 715-725.

MISICI, L. & ZIRILLI, F. 1994 Three-dimensional inverse obstacle scattering for time harmonic waves: A numerical method. SIAM J. Sci. Comput. 15, 1174-1189.

NORRIS, A. N. 1990 Resonant acoustic scattering from solid targets. J. Acoust. Soc. Am. 88, 505-

POTTHAST, R. 1996 A fast new method to solve inverse scattering problems. *Inverse Problems* 12, 731-742.

PRADA, C., THOMAS, J.-L., & FINK, M. 1995 The iterative time-reversal process: analysis of the convergence. *J. Acoust. Soc. Am.* 97, 62-71.

ROY, D. N. G., COUCHMAN, L., & WARNER, J. 1997 Scattering and inverse scattering of sound-hard obstacles via shape deformation. *Inverse Problems* 13, 589-606.

WATERMAN, P. C. 1968 Å new formulation of acoustic scattering. J. Acoust. Soc. Am. 45, 1417-1429.

Appendix A:. The function G for a circular target

The sum (3.45) has the explicit form in this case, using equation $(2.34)_2$,

$$G^{(N)}(\mathbf{x}_1, \mathbf{x}_2) = 2\pi \sum_{n=1}^{(N)} \frac{1}{\lambda_n} J_n(kr_1) J_n(kr_2) e^{in(\theta_1 - \theta_2)}.$$
 (A.1)

It is possible to make an accurate statement about the limiting behavior of this function as $N \to \infty$, assuming that no eigenvalue is identically zero. The eigenvalues λ_n can be found for large values of |n| by using the known properties $J_n(z) \approx (z/2)^n/n!$ and $H_n^{(1)}(z) \approx -\mathrm{i}(n-1)!(2/z)^n/\pi$, and assuming $\gamma \neq 0$, as

$$\lambda_n \approx \frac{-\mathrm{i}\pi}{|n|!(|n|-1)!} \left(\frac{ka}{2}\right)^{2|n|},\tag{A.2}$$

and therefore.

$$\frac{2\pi}{\lambda_n} J_n(kr_1) J_n(kr_2) \approx \frac{2\mathrm{i}}{|n|} \left(\frac{r_1 r_2}{a^2}\right)^{|n|} . \tag{A.3}$$

It is clear from equations (A.1) and (A.3) that the function $G = \lim_{N \to \infty} G^{(N)}$ is convergent if and only if $r_1 r_2 < a^2$. When this is the case we may sum the infinite part of the series by inspection, using $z + z^2/2 + z^3/3 + ... = \log \left[1/(1-z) \right]$, to give

$$G(\mathbf{x}_1, \mathbf{x}_2) = 2i \log \left[r_1^2 r_2^2 + a^4 - 2r_1 r_2 a^2 \cos(\theta_1 - \theta_2) \right] + G_0(\mathbf{x}_1, \mathbf{x}_2), \quad r_1 r_2 < a^2, \quad (A.4)$$

where G_0 is a bounded function for all $r_1r_2 \le a^2$. Equation (A.4) indicates that a logarithmic singularity occurs at the analyticity boundary $r_1r_2 = a^2$. Inside this domain the limiting function is bounded, while it is divergent for $r_1r_2 > a^2$.

It is interesting to note that the total field $p(\mathbf{x}, \mathbf{y})$ of equation (3.49) with $\mathbf{y} = \mathbf{x}$ is actually bounded if \mathbf{x} lies on the circle r = a. This can be seen from the fact that $H_0^{(1)}(z) \approx (i2/\pi) \log z$ as $z \to 0$. This is due to the fact that $\gamma \neq 0$, and the hard boundary condition dictates the limiting behaviour of G.

Appendix B:. Multiple scattering from circular obstacles

We consider $J \ge 2$ circular targets, of radii a_j and impedance γ_j , centred at \mathbf{x}_j , j = 1, 2, ..., J. Assuming that the incident wave is a plane wave in direction $\boldsymbol{\alpha}$, as in (2.1), then the total scattered solution is represented as

$$p^{s}(\mathbf{x}) = -\sum_{i=1}^{J} e^{ik\alpha \cdot \mathbf{x}_{j}} \sum_{n}^{N_{1}^{(j)}} \sum_{n}^{N_{2}^{(j)}} c_{nq}^{(j)} i^{n} H_{n}^{(1)}(kr_{j}) e^{i(n\theta_{j} - q\alpha)},$$
 (B.1)

where $\{r_j, \theta_j\}$ are polar coordinates of the field point **x** with respect to the centre of circle *j*. The far field follows from (2.4) and (B.1) as

$$u_{\infty}(\theta, \alpha) = \frac{1}{2\pi} \sum_{j=1}^{J} e^{-ik(\theta - \alpha) \cdot \mathbf{x}_{j}} \sum_{n=1}^{N_{1}^{(j)}} \sum_{q=1}^{N_{2}^{(j)}} c_{nq}^{(j)} e^{i(n\theta - q\alpha)}.$$
 (B.2)

The eigenvalues and eigenvectors can be determined from this by forming the matrix [U] of equation (4.53), which becomes in this case

$$U_{mp} = \sum_{j=1}^{J} \sum_{n=1}^{N_1^{(j)}} \sum_{q=1}^{N_2^{(j)}} c_{nq}^{(j)} i^{m-n-p+q} J_{n-m}(kr_{j0}) J_{q-p}(kr_{j0}) e^{-i(m-n-p+q)\theta_{j0}}, \quad (B.3)$$

where $\{r_{j0}, \theta_{j0}\}$ are polar coordinates of the centres \mathbf{x}_j , j=1,2,...,J with respect to the origin. It remains to determine the coefficients $c_{nq}^{(j)}$, which we do next.

The two main formulae required are

$$e^{ik\boldsymbol{\alpha}.\mathbf{x}} = e^{ik\boldsymbol{\alpha}.\mathbf{x}_j} \sum_{n=-\infty}^{\infty} i^n J_n(kr_j) e^{in(\theta_j - \alpha)},$$
 (B.4)

and

$$H_m^{(1)}(kr_l)e^{im\theta_l} = \sum_{n=-\infty}^{\infty} H_{m-n}^{(1)}(kr_{jl})e^{i(m-n)\theta_{jl}} J_n(kr_j)e^{in\theta_j},$$
 (B.5)

where $\{r_{jl}, \theta_{jl}\}\$ are the polar coordinates of \mathbf{x}_j relative to \mathbf{x}_l . Using these, we can write the total solution of (2.1) and (B.1) in terms of the coordinates of any one circle, thus:

$$p(\mathbf{x}) = e^{ik\boldsymbol{\alpha}.\mathbf{x}_j} \sum_{n} b_n^{(j)}(r_j, \alpha) i^n e^{in\theta_j},$$
 (B.6)

where

$$b_n^{(j)}(r_j, \alpha) = J_n(kr_j)e^{-in\alpha} - \sum_{q}^{N_2^{(j)}} c_{nq}^{(j)} e^{-iq\alpha} H_n^{(1)}(kr_j)$$

$$-J_n(kr_j) \sum_{l \neq j}^{J} e^{ik\alpha \cdot (\mathbf{x}_l - \mathbf{x}_j)} \sum_{m}^{N_1^{(l)}} \sum_{q}^{N_2^{(l)}} c_{mq}^{(l)} e^{-iq\alpha} i^{m-n} H_{m-n}^{(1)}(kr_{jl}) e^{i(m-n)\theta_{jl}}.(B.7)$$

This form allows us to apply the boundary condition (2.3) on obstacle j ($r_j = a_j$) as a series in $e^{in\theta_j}$, and equating each coefficient to zero, we obtain

$$0 = \lambda_n^{(j)} e^{-in\alpha} - \sum_{q}^{N_2^{(j)}} c_{nq}^{(j)} e^{-iq\alpha}$$
$$-\lambda_n^{(j)} \sum_{l \neq j}^{J} e^{ik\alpha \cdot (\mathbf{x}_l - \mathbf{x}_j)} \sum_{m}^{N_1^{(l)}} \sum_{q}^{N_2^{(l)}} c_{mq}^{(l)} e^{-iq\alpha} i^{m-n} H_{m-n}^{(1)}(kr_{jl}) e^{i(m-n)\theta_{jl}}, \quad (B.8)$$

where $\lambda_n^{(j)}$ is the far field eigenvalue associated with obstacle j in the absence of the others, that is,

$$\lambda_n^{(j)} = \frac{J_n(ka_j) + k\gamma_j J'_n(ka_j)}{H_n^{(1)}(ka_j) + k\gamma_j H_n^{(1)'}(ka_j)}.$$
(B.9)

Now take the inner product of (B.8) with $e^{iq\alpha}$ for each q, to get a linear system of equation for the unknowns $c_{nq}^{(j)}$,

$$c_{nq}^{(j)} + \lambda_n^{(j)} \sum_{l \neq j}^{J} \sum_{m}^{N_1^{(l)}} \sum_{p}^{N_2^{(l)}} c_{mp}^{(l)} i^{m-n-p+q} H_{m-n}^{(1)}(kr_{jl}) J_{p-q}(kr_{jl}) e^{i(m-n-p+q)\theta_{jl}} = \lambda_n^{(j)} \delta_{nq}.$$
(B.10)

In the computations reported $N_1^{(j)}=N_1$ and $N_2^{(j)}=N_2$ with $N_1=N_2$. The solution was obtained using MATLAB, which handles the equations very expeditiously. For instance, the matrix in (B.10) is formed by first forming two separate $N_1\times N_2$ matrices and then using the kron function within MATLAB to generate the large $N_1N_2J\times N_1N_2J$ matrix. The linear system in the N_1N_2J unknowns $c_{nq}^{(j)}$ was solved directly when the size was not too great ($\leq 10^3$) or when the frequency was high. Iteration was used for large systems and for low frequencies. The iterative procedure rewrites the system as (I-M)L=R, and solves for L as L=R+MR+M(MR)+... Once the unknowns is found, then the [U] matrix is determined from (B.3) as

$$[U] = \sum_{j=1}^{J} [A^{(j)}][C^{(j)}][A^{(j)}]^*, \qquad A_{mn}^{(j)} = i^{m-n} e^{i(n-m)\theta_{j0}} J_{n-m}(kr_{j0}).$$
 (B.11)

In this way the vectorization capabilities of MATLAB can be used to advantage.